

Investigation of Dominant Wave Mechanism and Optimal Antenna Excitation for Body-Centric Wireless Propagations

Daniel U. Agu^{1, *}, Mary Leece¹, Jose Alcala-Medel¹, Anna Sahdev¹, Jim Lim¹,
Matthew Olsen¹, Bithiah Ngan¹, Youngwook Kim², and Yang Li¹

Abstract—Vertically- and horizontally-polarized antennas were investigated for on-body to on-body (OB2OB), in-body to in-body (IB2IB), and on-body to in-body (OB2IB) wireless propagations at frequencies of 915 MHz and 2.45 GHz. Theoretical formulations, simulations, and measurements were employed to study the effect of source antenna orientation on the attenuation of the radio frequency (RF) wave as it propagates around, inside, and through the body near the torso region. The results show that the vertical polarization is preferred for OB2OB communication, and the horizontal polarization is better for IB2IB communication. Furthermore, the dominant propagation mechanism and optimum antenna excitation for OB2IB communication are identified to be distance-dependent. The horizontally-polarized dipole is preferred at a shorter distance while the vertically-polarized dipole is preferred at a larger distance away from the source. The observed results were explained using the estimated attenuation rates of the different propagation mechanisms.

1. INTRODUCTION

With the latest advance of wearable technology, more and more miniaturized and power-efficient sensors are being deployed over the human body surface for health monitoring purposes. These sensors can continuously collect our physiological data and wirelessly relay the information to a data hub (e.g., smartphone) for further processing. Such technological advances will transform the health industry practice from the current office visit-based mode to a remote patient monitoring-based mode. To ensure a reliable and efficient communication link between wearable sensors and the data hub, researchers have thoroughly investigated on-body to on-body (OB2OB) wireless channels. Two dominant on-body channel propagation mechanisms have been identified: ground waves for the line-of-sight (LOS) propagation and creeping waves for the non-LOS (NLOS) propagation [1]. The creeping wave propagation experiences exponential decay and its propagation characteristics have been studied using full-wave simulations [2], theoretical formulation [3], and in-situ experimental trials [4]. Ryckaert et al. [2] first reported the creeping wave mechanism by collecting electric field distributions around a human phantom model using a finite-difference time-domain (FDTD) simulation approach. He also confirmed the simulation results by measurements performed on real human subjects. Wait [5] developed the creeping wave theory on a curved surface, and Alves et al. [3] applied it to around-body propagations. Xue et al. [6] also investigated broadband on-body wave propagations and extracted the dominant wave mechanisms and their propagation constants.

In addition to the proliferation of wearable sensors, implanted and ingested sensors have become increasingly popular in biomedical and health industries. These sensors can collect real-time biological information such as glucose level, heart activity and tumor growth for health monitoring purposes. For

Received 16 May 2020, Accepted 27 June 2020, Scheduled 9 July 2020

* Corresponding author: Daniel U. Agu (danielLagu@baylor.edu).

¹ Department of Electrical and Computer Engineering, Baylor University, Waco, TX 76798, USA. ² Department of Electrical and Computer Engineering, California State University, Fresno, CA 93740, USA.

in-body to in-body (IB2IB) communication, the study is more challenging because of the complicated environment inside the human body. To address this problem, not only sophisticated and innovative 3D human voxel models have been created, but also simulation tools have been developed to study radio frequency (RF) wave propagations from radio implants [7]. Apart from virtual platforms, physical body phantoms which can be in liquid, semisolid (gel) or solid form have been developed for in-body communication studies [1]. Also, robust antenna designs are desired to improve radiation efficiency and prevent detuning in this environment [8–10]. For IB2IB communication, the dominant propagation mechanism is found to be a direct path between transmitting and receiving antennas. Kurup et al. [11] proposed an in-body path loss model for homogeneous human tissue at 2.4 GHz. Alomainy [12] models and characterizes a wireless radio channel from ingested implants considering the structures and dielectric constants of organs. Furthermore, a statistical path loss model has been developed to explain the in-body wireless propagations [13].

Apart from OB2OB and IB2IB communication, there is also a wireless propagation channel between a wearable sensor and an implanted sensor, also known as the on-body to in-body (OB2IB) propagation channel. A few studies have been performed on OB2IB propagation channel. For example, an OB2IB path loss model [13] has been applied for in-body localization to advance technologies such as Wireless Capsule Endoscopy (WCE), a method to visualize and diagnose the human gastrointestinal tract [7]. However, the dominant propagation mechanism for the OB2IB channel has yet to be identified, and the optimum antenna orientation which can maximize the OB2IB signal transmission has not been discussed. In this research work, we aim to answer these two scientific questions by carefully comparing the OB2OB and IB2IB wave characteristics which we employ to explain the OB2IB wave characteristics. The study is performed at two commonly used ISM frequency bands: 915 MHz and 2.45 GHz.

This paper is organized as follows. In Section 2, the OB2OB wave propagation is reviewed for both vertically- and horizontally-oriented transmitting antennas. Analytical derivations, numerical simulations and real human measurements are performed to determine the attenuation rates of the dominant propagation mechanism. In Section 3, the IB2IB propagation is investigated using numerical simulations. For the measurement, a liquid phantom model is also created, and the measurement results are compared against simulation results. The wave attenuation constants are compared between OB2OB and IB2IB cases. In Section 4, the OB2IB propagation is studied based on both simplified and realistic human phantom models. The dominant wave mechanism and its associated antenna excitation are identified. Section 5 summarizes the paper.

2. OB2OB WAVE PROPAGATION AND ANTENNA EXCITATION

The previous OB2OB propagation studies have just focused on creeping waves excited by a vertically-polarized antenna source. There is limited work on the horizontal-polarized antenna source [14]. In this research work, we first present the theoretical model of electric field distributions for both types of polarizations, from which we extract the wave attenuation constants. The theoretical models were

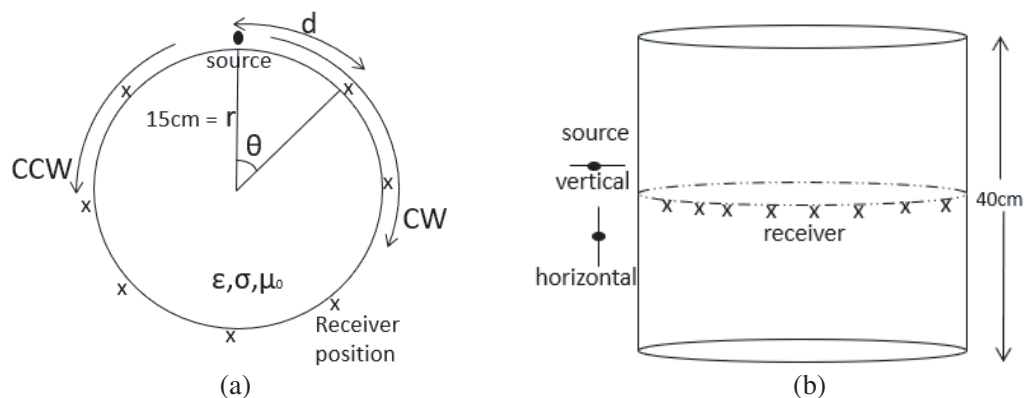


Figure 1. OB2OB cylinder model. (a) Top view. (b) Side view.

derived based on Wait's theory [5]. For this model, the human torso was modelled as a homogeneous cylinder of radius 15 cm and height 40 cm filled with tissue properties equivalent to muscle [15]. Previous studies have shown that a homogeneous cylinder model filled with muscle or 2/3 muscle can be a good representation of a real human torso for OB2OB propagation research [3, 4, 6].

As shown in Fig. 1(a), for an antenna source placed on the surface of the cylinder, two creeping waves are excited and travel in opposite directions (clockwise (CW) and counter-clockwise (CCW) creeping waves) from the source antenna, since the dipole radiates isotropically in the azimuth direction. The source antenna can be placed either in the x -direction (defined as a vertical dipole that is perpendicular to the surface of the cylinder) or in the z -direction (defined as a horizontal dipole that is in parallel to the surface of the cylinder). The radiated electromagnetic waves are then received by the receiving antenna placed around the cylinder surface at the observation points as shown in Fig. 1(b). The radiated electric fields from the antenna source were given in [14], which consists of both dominant and higher-order creeping wave modes. The expressions of the dominant mode are extracted as follows:

$$E_{v,h} = \frac{j\omega \cdot \mu_0 \cdot I \cdot dl}{2\pi} \cdot \frac{e^{-\frac{j\omega d}{c}}}{d} \cdot e^{-\frac{j\pi}{4}} \cdot \sqrt{\pi\xi} \cdot \frac{W^2 \left(\tau_1^{v,h} - \sqrt[3]{\frac{2}{k_0 r}} k_0 h \right)}{W^2 \left(\tau_1^{v,h} \right) \left(\tau_1^{v,h} - q_{v,h}^2 \right)} \cdot e^{-j\xi\tau_1^{v,h}} \quad (1)$$

where,

$$W(\tau) = \sqrt{\pi} [B_i(\tau) - jA_i(\tau)] \quad (2)$$

$$\xi = \sqrt[3]{\frac{\omega r}{2c}} \frac{d}{r} \quad (3)$$

$$q_v = -j\sqrt[3]{\frac{\omega r}{2c}} \sqrt{\frac{1}{\varepsilon}} \quad q_h = -j\sqrt[3]{\frac{\omega r}{2c}} \sqrt{\varepsilon} \quad (4)$$

$$W' \left(\tau_1^{v,h} \right) - q_{v,h} W \left(\tau_1^{v,h} \right) = 0 \quad (5)$$

E_v and E_h denote the electric fields excited by the vertical dipole and horizontal dipole, respectively. r is the radius of the cylinder, h the height of the source and receiver above the cylinder, and d the distance around the cylinder from the source antenna (i.e., arc distance). For the CW case, $d = r\theta$ and for the CCW case, $d = r(2\pi - \theta)$. $I dl$ is the dipole moment, k_0 the wave number in free space, μ_0 the permeability of free space, c the speed of light in free space, and ε the complex permittivity of the muscle medium. $\tau_1^{v,h}$ is the first root obtained by solving Eq. (5), which depends on the operating frequency and radius of the cylinder. A_i and B_i represent Airy-Fock functions of the first and second kind, respectively, which are employed in the definition of the function $W(\tau)$ in Eq. (2).

To verify the above theoretical model, we simulate the electric fields around a homogenous cylinder using FEKO, a method of moment (MoM) tool. We used near field probes in FEKO to collect the electric field intensities for both near and far field regions. The cylinder is filled with tissue of dielectric constants equivalent to muscle ($\varepsilon_r = 54.9$ and $\sigma = 0.95$ S/m at 915 MHz; and $\varepsilon_r = 52.7$ and $\sigma = 1.73$ S/m at 2.45 GHz) [15]. The radius and height of the cylinder are 15 cm and 40 cm. The antennas of length 15.63 cm at 915 MHz and 5.56 cm at 2.45 GHz are positioned 2 cm away from the cylinder and the electric fields are collected every 1 mm along the displayed curved path in the figure (Fig. 1(b)). Figs. 2(a) and (b) show the distributions of electric fields at 915 MHz and 2.45 GHz, respectively. The theoretical and simulation results show good agreement with each other. It is seen that the waves excited by the horizontal antenna source are much weaker and decay much faster than those of the vertical antenna source. The attenuation rate of the electric field can be extracted from the linear region of the plot by using linear least-square fitting. At 915 MHz, the attenuation rates are found to be 0.84 dB/cm and 1.40 dB/cm for the vertical and horizontal dipole sources; and at 2.45 GHz, the attenuation rates are 1.00 dB/cm and 1.92 dB/cm for the vertical and horizontal dipole sources.

To corroborate with the above theory and simulation findings, we measured the path loss around a human volunteer of height 183 cm and torso circumference of 82.5 cm using vertically- and horizontally-oriented dipole antennas in an indoor environment. Fig. 3 shows the experimental setup. The vertical (horizontal) transmitting antenna is fixed in front of the navel, and the vertical (horizontal) receiving antenna is moved around the torso at an increment of 2.5 cm. The transmission data S_{21} is measured

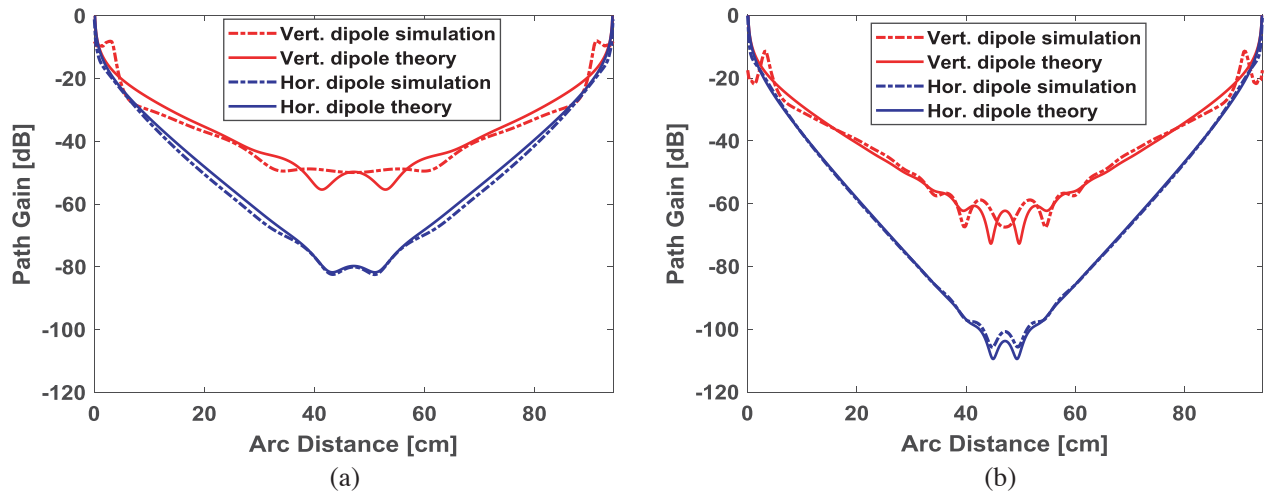


Figure 2. Creeping wave E -field pattern. (a) 915 MHz, (b) 2.45 GHz.

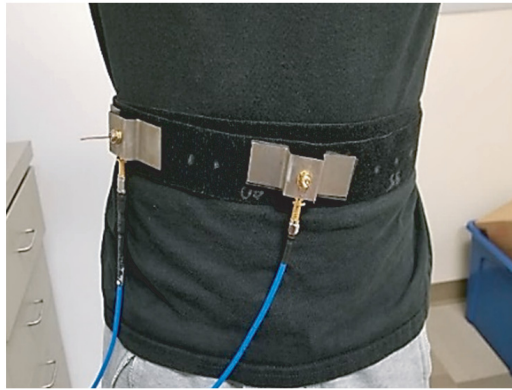


Figure 3. OB2OB experimental setup.

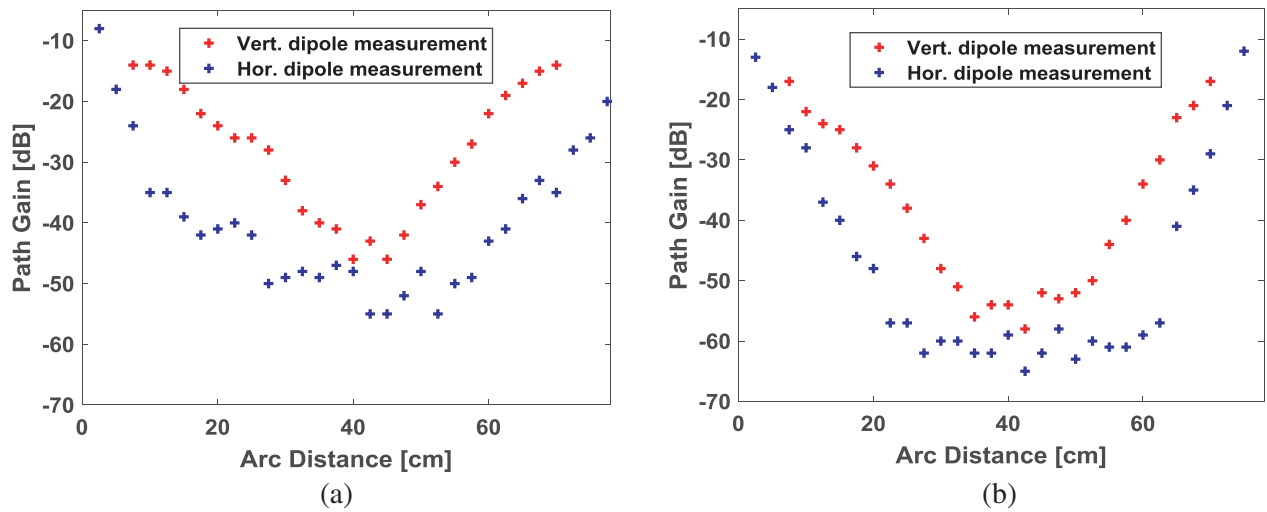


Figure 4. Creeping wave E -field pattern around human (a) 915 MHz (b) 2.45 GHz.

using a vector network analyzer (FieldFox N9923A). Figs. 4(a) and (b) show the results at 915 MHz and 2.45 GHz, respectively. Similar to the simulation and theory results, the measurements show that the creeping waves excited by the vertical source decay slower than those of the horizontal source. However, the path loss difference between the vertical and horizontal antennas is not as significant as those of the theory and simulation because of presumably the multipath effects from the measurement environment.

3. IB2IB WAVE PROPAGATION AND ANTENNA EXCITATION

In this section, we study the in-body propagation for both vertical and horizontal sources using simulation and measurement approaches, and then compare the results with the OB2OB cases. The simulation setup and cylinder model are similar to Fig. 1(b), except that the transmitting and receiving antennas are now placed inside the muscle-filled cylinder, as shown in Fig. 5. The antennas are bare dipoles of length 4.8 cm at 915 MHz, and insulated half-wave dipoles of length 5.3 cm at 2.45 GHz. We use the insulated dipole at 2.45 GHz to increase the antenna radiation efficiency since the signal transmission loss at 2.45 GHz is much larger than that at 915 MHz. At 2.45 GHz, the insulation layer is air in the simulation with layer thickness of 0.3 cm. The radius of the dipole is 0.0405 cm at both frequencies. The reflection coefficients of the dipole antennas are below -10 dB at the resonance frequencies of 915 MHz and 2.45 GHz. The radiated electric fields are collected by the receiving antenna along a straight line inside the cylinder at an interval of 1 mm.

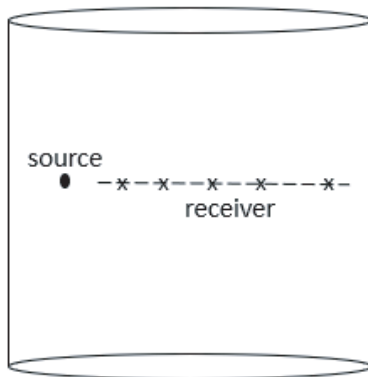


Figure 5. IB2IB cylinder model.

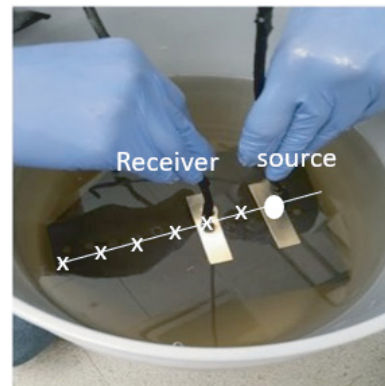


Figure 6. Phantom solution in cylinder bucket.

To verify the simulation, the experiment is carried out as well. We use the Agilent PNA N5320C vector network analyzer (VNA) for measurements. A liquid muscle phantom solution consisting of distilled water, sugar, and salt [16, 17] is produced in the lab, and its dielectric constants ($\epsilon_r = 53.67$ and $\sigma = 1.21$ S/m at 915 MHz; and $\epsilon_r = 49.88$ and $\sigma = 2.66$ S/m at 2.45 GHz) are measured using a dielectric probe. The liquid is then used to fill in a cylinder bucket of radius 15 cm, as shown in Fig. 6. Similar to the simulations, air-insulated dipole antennas are also used at 2.45 GHz while bare dipoles are used at 915 MHz. In the experiment, teflon is used as a thin insulating sheath for the air insulation layer in the 2.45 GHz case. The sizes of the antennas are the same as in the simulations. In the measurement the transmitting antenna is fixed while the receiving antenna is moved at increments of 5 mm (except for the horizontal dipole at 915 MHz where the separation was 2 cm) until the end of the cylinder or the noise floor of the VNA is hit.

Figures 7(a) and (b) plot the normalized electric field distributions at 915 MHz and 2.45 GHz. The plots contain both simulation and measurement data which show good agreement at 915 MHz and a fairly good agreement at 2.45 GHz owing to noise effects. The noise effect from the environment at 2.45 GHz became prominent as separation between source and receiver increased more than 12 cm for the horizontal orientation case and 9 cm for the vertical orientation case. From Fig. 7, at 915 MHz, the field radiated by the vertical dipole source is much weaker than the horizontal source, which can be mainly attributed to the radiation pattern of the antenna. The attenuation constants for the vertical

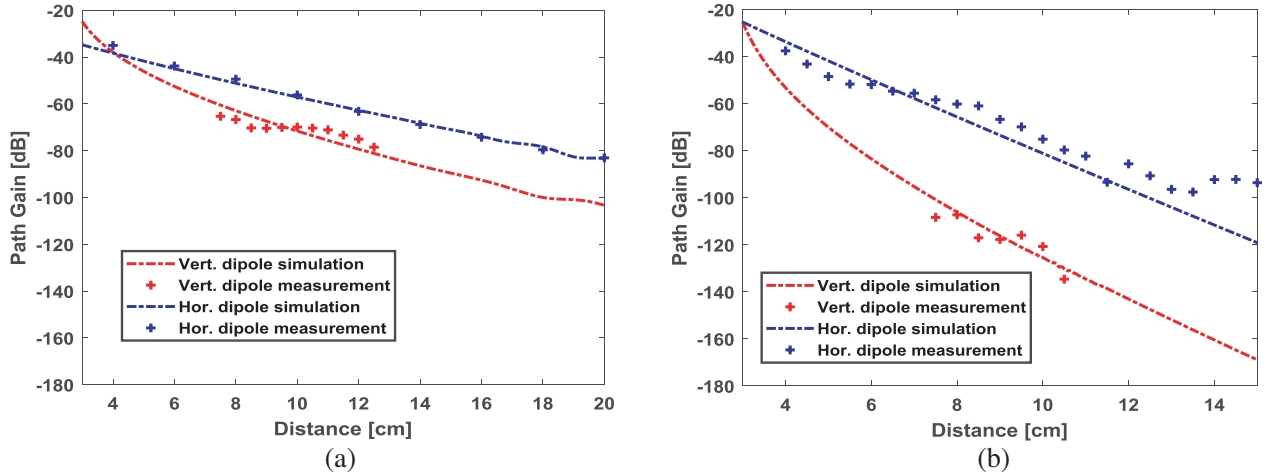


Figure 7. *E*-field pattern inside the body. (a) 915 MHz, (b) 2.45 GHz.

source (3.20 dB/cm) is also larger than that of the horizontal dipole source (2.72 dB/cm). Similar observations can also be made at 2.45 GHz, whereby the attenuation constant for the vertical source (9.20 dB/cm) is greater than that of the horizontal dipole source (7.69 dB/cm).

It is worthwhile to make a quantitative comparison between the OB2OB creeping wave attenuation and the IB2IB direct path attenuation. Table 1 summarizes the extracted exponential attenuation constants from the full-wave simulations of the OB2OB and IB2IB cases, considering both vertical and horizontal transmitting antenna sources. On the first observation, the IB2IB attenuation constants are much larger than the OB2OB attenuation constants because of the lossy nature of the muscle tissue. Secondly, the optimum transmitting antennas are found to be vertically-oriented (normal to the body surface) antennas for the OB2OB propagation and horizontally-oriented (parallel to the body surface) antennas for the IB2IB propagation. Lastly, as the frequency increases, the attenuation constants increase slightly for the OB2OB creeping waves, but significantly for the IB2IB propagations. These observations will help identify and explain the OB2IB wave propagations in the next section.

Table 1. Comparison of attenuation rates.

Vertical/horizontal (dB/cm)	915 MHz	2.45 GHz
OB2OB	0.84/1.41	1/1.92
IB2IB	3.2/2.72	9.2/7.69

4. OB2IB WAVE PROPAGATION AND ANTENNA EXCITATION

In this section, we extend the above OB2OB and IB2IB research into the OB2IB study, with the goal of identifying the dominant propagation path and its associated optimum source antenna orientation. The muscle-filled human torso cylinder model of radius 15 cm and height 40 cm presented in Sections 2 and 3 will be used first to simulate the OB2IB wave propagations. The side view of the simulation setup is shown in the Fig. 8. The source antennas having the same dimensions as the OB2OB study are placed outside but close to the body surface for both the vertical and horizontal configuration, and their radiated electric fields are simulated both inside and outside of the cylinder. The on-body antenna size and geometry are the same as in the OB2OB study.

Figure 9 shows the 915 MHz normalized electric field distributions for the vertical and horizontal antenna sources, respectively. For the vertical antenna field source, as shown in the Fig. 9(a), it is seen the

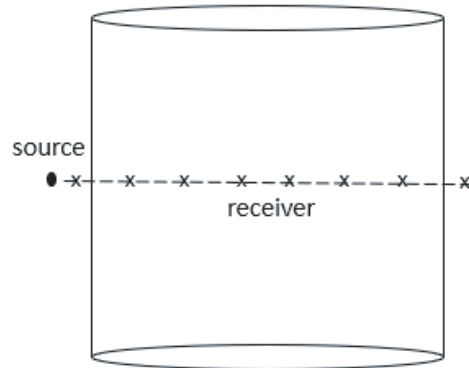


Figure 8. OB2IB cylinder model.

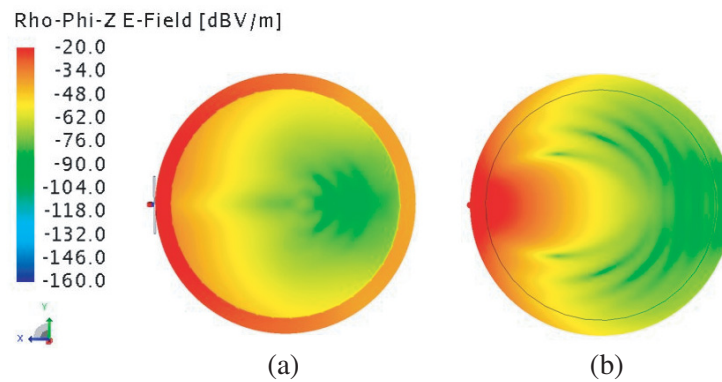


Figure 9. Colormap of E -field at 915 MHz. (a) Vertical configuration. (b) Horizontal configuration.

field strength around the cylinder is stronger than the field inside of it since: (i) the dominant electric field component E_ρ is not continuous at the boundary of the cylinder surface; (ii) the on-body creeping wave is strongly excited by the vertical source and decays much slower than the in-body direct path (attenuation rates of 0.84 dB/cm vs. 3.2 dB/cm). For the horizontal antenna source, as shown in the Fig. 9 (b), the fields around the cylinder are still stronger than the fields inside the cylinder, but the strength difference is smaller because: (i) the dominant electric field component E_z is continuous at the boundary of cylinder surface; (ii) the attenuation constants of creeping wave and the direct path are closer to each other (attenuation rates of 1.41 dB/cm vs. 2.72 dB/cm).

The above observations are even more noticeable in Fig. 10, which shows the 2.45 GHz normalized electric field distributions for vertical and horizontal antenna sources, respectively. The field strengths around the cylinder are much larger than the field strength inside of the cylinder for both vertical and horizontal dipoles because as frequency increases, the attenuation constants increase slightly for the creeping waves, but significantly for the in-body direct path, as shown in the Table 1. In fact, we can see the field strength at point B is much stronger than that at point A even though the location of B is further away from the source antenna.

To make a more quantitative comparison, the normalized electric fields are plotted along the x -axis for both vertical and horizontal sources, as shown in Fig. 11(a) and Fig. 11(b). The plots show the field strength both outside and inside of the cylinder at its center height ($z = 20$ cm). The boundaries of the cylinder surfaces are located at $x = 2$ and $x = 32$ cm. For Fig. 11(a), the field decays fast as the distance away from the source increases, similar to the IB2IB case discussed in Section 3; however, it stops decaying and even shows the increase of its value as the receiving point moves towards the back of the cylinder. The increase of the field strength can be attributed to the creeping wave contributions since it experiences much less decay than the in-body direct path. This pattern of switching is even more pronounced in Fig. 11(b), as the difference between direct path decay and creeping wave decay

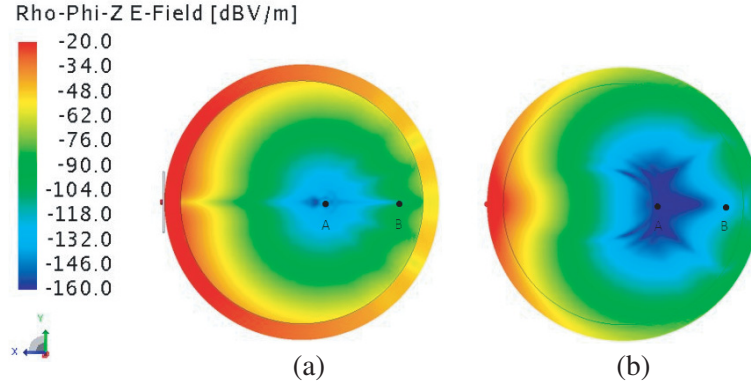


Figure 10. Colormap of E -field at 2.45 GHz. (a) Vertical configuration. (b) Horizontal configuration.

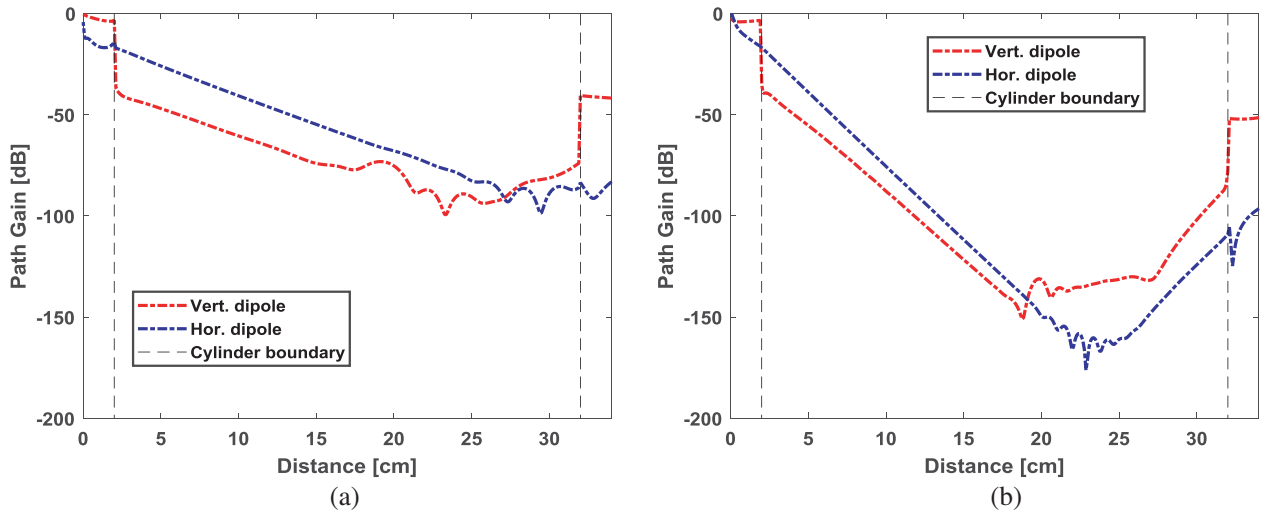


Figure 11. OB2IB E -field pattern. (a) 915 MHz. (b) 2.45 GHz.

becomes larger at higher frequencies.

It is also seen from Fig. 11(a) and Fig. 11(b) that the horizontal antenna source is preferred for OB2IB propagation when the receiving sensor is placed at short distances away from the source and the direct path is the dominant wave mechanism. On the other hand, it is better to use a vertical antenna source at a large distance away from the source and when the creeping wave is the dominant wave mechanism.

It would be interesting to see whether we can make similar observations in the experimental trial using our liquid phantom model. However, the RF signal decays so fast in the lossy liquid that we are unable to measure the signal below the VNA noise floor. Instead, we use a realistic human voxel model to perform a similar simulation at 915 MHz in order to confirm the above observations. We were unable to perform the voxel simulation at 2.45 GHz due to computational limitations. The inhomogeneous model was obtained from the full body visible human project. The model is a male subject of height 181 cm with an optimized antenna of length 15.41 cm positioned where a 30 cm line segment fits between the front and back of the body. The model is shown in Fig. 12 The model consisted 2.2 million 8 mm sized tetrahedral voxels and comprised 27 different tissues. The solution was obtained using the FDTD simulation approach.

The comparison between the horizontal and vertical configurations is shown in Fig. 13. The simulation results are similar to the simplified cylinder results in Fig. 11(a). The horizontal antenna source and its associated direct path are preferred at short distances while the vertical antenna source

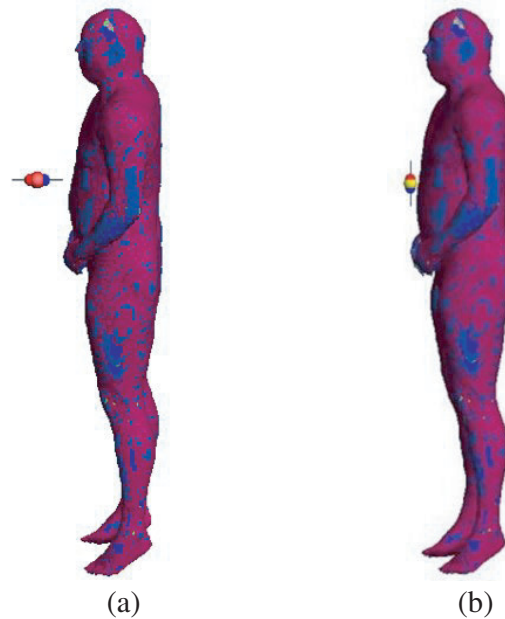


Figure 12. OB2IB realistic voxel model. (a) Vertical configuration. (b) Horizontal configuration.

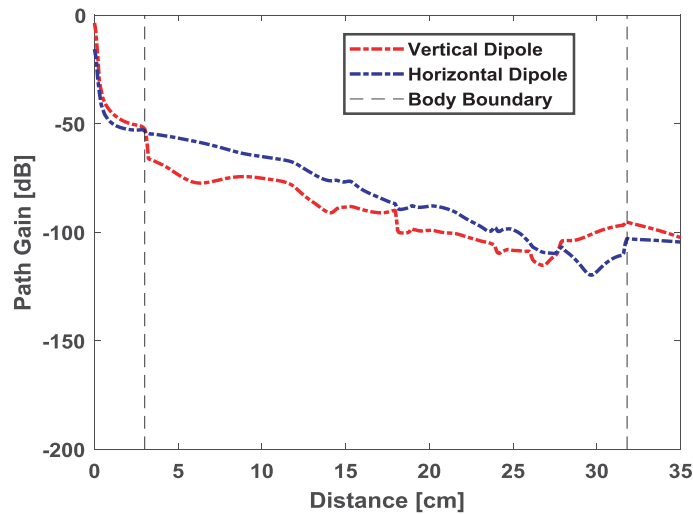


Figure 13. Voxel model OB2IB *E*-field pattern at 915 MHz.

and its associated creeping wave path are preferred at large distances. It is interesting to observe that the switching point occurs at around 27 cm similar to the result obtained in Fig. 11(a).

We would like to draw an analogy between the OB2IB propagation and the wave propagations in a forest environment. It is well-known that at HF frequency range, the forest can be described using a lossy, equivalent slab model [18, 19]. For short distance between transmitting and receiving antennas, the direct path is the dominant propagation mechanism. Over the large distance, however, the lateral wave propagating along the top of the slab is the dominant propagation path. The creeping wave propagation around the human body plays a similar role as the lateral wave propagation over the tree tops.

5. CONCLUSION

In this paper, we compared between OB2OB and IB2IB wave propagations through theory, simulations, and measurements. It is found that the on-body creeping wave experiences much less decay than the in-body direct path. It is also confirmed that a vertical antenna source is more suitable for creeping wave excitation while a horizontal antenna source is preferred for in-body direct path.

We also identified the dominant OB2IB wave mechanisms and the optimum antenna sources which can excite them. It is found that when the in-body receiving antenna is placed at a short distance away from the on-body transmitting antenna, the direct path is the dominant wave mechanism and a horizontal-polarized antenna source parallel to the body surface is preferred to use. On the other hand, when the in-body receiving antenna is placed at a large distance away from the on-body transmitting antenna, the creeping wave path is the dominant wave mechanism and a vertical-polarized antenna source perpendicular to the body surface is preferred to use. These findings are verified using full-wave simulations over both simplified and realistic human phantom model.

For future work, we will investigate the OB2IB channel perturbations during human motions and the design of optimum on-body and in-body antennas, and conduct more voxel simulation studies at GHz microwave frequencies.

REFERENCES

1. Hall, P. S. and Y. Hao, *Antennas and Propagation for Body-Centric Wireless Communications*, Artech House, London, UK, 2006.
2. Ryckaert, J., et al., "Channel model for wireless communication around human body," *Electronics Letters*, Vol. 40, No. 9, 543–544, 2004.
3. Alves, T., B. Poussot, and J. M. Laheurte, "Analytical propagation modeling of BAN channels based on the creeping-wave theory," *IEEE Transactions on Antennas and Propagation*, Vol. 59, No. 4, 1269–1274, 2011.
4. Bresnahan, D. and Y. Li, "Investigation of creeping wave propagation around the human head at ISM frequencies," *IEEE Antennas and Wireless Propagation Letters*, Vol. 16, 2767–2770, 2017.
5. Wait, J. R., "On the excitation of electromagnetic surface waves on a curved surface," *IRE Transactions on Antennas and Propagation*, Vol. 8, No. 4, 445–448, 1960.
6. Xue, D., B. A. Garner, and Y. Li, "Investigation of short-range, broadband, on-body electromagnetic wave propagations," *IET Microwaves, Antennas & Propagation*, Vol. 10, No. 11, 1182–1188, 2016.
7. Pourhomayoun, M., M. Fowler, and Z. Jin, "A novel method for medical implant in-body localization," *2012 Annual International Conference of the IEEE Engineering in Medicine and Biology Society*, 5757–5760, San Diego, CA, USA, 2012.
8. Bhattacharjee, S., S. Maity, S. R. B. Chaudhuri, and M. Mitra, "A compact dual band dual polarized omnidirectional antenna for ON body alications," *IEEE Transactions on Antennas and Propagation*, Vol. 67, No. 8, 5044–5053, 2019.
9. Bhattacharjee, S., S. Maity, S. R. B. Chaudhuri, and M. Mitra, "Metamaterial-inspired wideband biocompatible antenna for implantable alications," *IET Microwaves, Antennas & Propagation*, Vol. 12, No. 11, 1799–1805, 2018.
10. Maity, S., K. R. Barman, and S. Bhattacharjee, "Silicon-based technology: Circularly polarized microstrip patch antenna at ISM band with miniature structure using fractal geometry for biomedical alication," *Microwave and Optical Technology Letters*, Vol. 60, No. 1, 93–101, 2018.
11. Kurup, D., et al., "In-body path loss model for homogeneous human tissues," *IEEE Transactions on Electromagnetic Compatibility*, Vol. 54, No. 3, 556–564, 2011.
12. Alomainy, A. and Y. Hao, "Modeling and characterization of biotelemetric radio channel from ingested implants considering organ contents," *IEEE Transactions on Antennas and Propagation*, Vol. 57, No. 4, 999–1005, 2009.

13. Sayrafian-Pour, K., et al., "A statistical path loss model for medical implant communication channels," *2009 IEEE 20th International Symposium on Personal, Indoor and Mobile Radio Communications*, 2995–2999, Tokyo, Japan, 2009.
14. Petrillo, L., et al., "Analytical creeping wave model and measurements for 60 GHz body area networks," *IEEE Transactions on Antennas and Propagation*, Vol. 62, No. 8, 4352–4356, 2014.
15. "Internet resources of biological tissue properties," Available at <http://niremf.ifac.cnr.it/tiss-prop/htmlclie/htmlclie.php>.
16. Forbes, R. M., A. R. Cooper, and H. H. Mitchell, "The composition of the adult human body as determined by chemical analysis," *J. Biol. Chem.*, Vol. 203, No. 1, 359–366, 1953.
17. "Dielectric phantom recipe generator," Available at <https://amri.ninds.nih.gov/cgi-bin/phantomrecipe>.
18. Tamir, T., "Radio wave propagation along mixed paths in forest environments," *IEEE Transactions on Antennas and Propagation*, Vol. 25, No. 4, 471–477, 1977.
19. Li, Y., M. F. Wu, A. E. Yilmaz, and H. Ling, "Investigation of short-range radiowave propagation at HF/VHF frequencies in a forested environment," *IEEE Antennas and Wireless Propagation Letters*, Vol. 8, 1182–1185, 2009.